

## Research Paper

## Modeling acoustic emission in the Brazilian test using moment tensor inversion

Jun Ma<sup>a,c</sup>, Shunchuan Wu<sup>a,b,\*</sup>, Xiao-Ping Zhang<sup>d</sup>, Yixiang Gan<sup>c</sup><sup>a</sup> Key Laboratory of Ministry for Efficient Mining and Safety of Metal Mines, University of Science and Technology Beijing, Beijing 100083, China<sup>b</sup> Faculty of Land Resource Engineering of KUST, Kunming University of Science and Technology, Kunming 650093, China<sup>c</sup> School of Civil Engineering, The University of Sydney, Sydney, NSW 2006, Australia<sup>d</sup> The Key Laboratory of Safety for Geotechnical and Structural Engineering of Hubei Province, School of Civil Engineering, Wuhan University, Wuhan 430072, China

## ARTICLE INFO

**Keywords:**  
 Brazilian test  
 Crack propagation  
 Acoustic emission  
 Moment tensor

## ABSTRACT

To investigate the crack propagation and failure mechanisms of brittle materials in the Brazilian tests, an acoustic emission (AE) simulation was implemented in the Discrete Element Method. AE location and magnitude were monitored during the whole process of the simulation to detailedly observe crack initiation and associated AE evolution. Moment tensors were directly calculated by the forces and motions of the particles and decomposed into isotropic and deviatoric parts. According to the decomposition results of moment tensors, AE events (microcracks) can be classified into explosive (tensile), shear and implosive sources. Explosive sources were found to dominate both the total number and energy emission, followed by shear sources and finally implosive sources. AE distributions of different AE types were compared with the stress distribution to explore the relation between failure evolution and intrinsic stress state of the Brazilian test. Furthermore, the approach was applied to the compression test with a single flaw. Comparisons with experimental results indicated that the AE simulation can overcome the shortcoming of signal missing near the peak load in experiments and is approved to be an effective and accurate way to study rock fracture mechanism.

## 1. Introduction

Due to the limitations of direct tensile tests for rock, the Brazilian test, an indirect method, was recommended by ISRM to determine the tensile strength of the rock in 1978 and has been widely used up to now. However, special attentions should be paid to the results from Brazilian tests for cases when the crack initiation point occurs away from the center of the disk. Some research indicates that the Brazilian test may underestimate the tensile strength of rocks [1–4], while some considered that the Brazilian test could reflect the true tensile strength of rocks [5,6], but the great majority of studies considered that the Brazilian test overestimated the tensile strength of rocks [4,7–9]. Such discrepancy can be traced back to the stress state experienced by samples undergoing Brazilian tests. Unlike the uniaxial stress state of the direct tensile test, the Brazilian disk is subjected to a triaxial stress state. Some researchers thought that the Brazilian test can never replace the direct tensile test, however, the compression induced tensile stress, e.g., in hydraulic fracturing or around tunnels, etc., is much more often presenting in practical applications while a pure tension state rarely presents. Thus, the Brazilian test is useful for understanding the failure

process and fracture mechanism of rocks. The key questions here remain on how cracks initiate and propagate through the disk and the relation between crack evolution and stress state.

Several approaches have been adopted to study the fracture mechanism in the Brazilian test. Fairhurst [1] theoretically analyzed the stress distribution in the Brazilian test based on the empirically generalized Griffith criterion and indicated that shear failure may occur away from the center of the disk using the Mohr envelope. Van De Steen et al. [10] loaded a Brazilian disk with a hole, which was drilled parallel to the sample axis and centered on the diameter perpendicular to the loaded diameter, and proposed that fracturing is initiated in shear near one of the platens and subsequently grows in tension in the Brazilian test. Lanaro et al. [11] used numerical method based on the Mohr-Coulomb criterion with a tension cut-off and stated that the failure might occur in tension and shear. Li and Wong [12] numerically found that the crack may initiate near the loading point in the Brazilian test for rocks according to the critical extension strain criterion. However, various strength criteria have different emphases on selective failure modes, for example, Mohr-Coulomb criterion mainly takes into account shear failure, instead, Griffith criterion only allows cracks to break in

\* Corresponding author.

E-mail addresses: [mingo\\_mj@outlook.com](mailto:mingo_mj@outlook.com) (J. Ma), [wushunchuan@ustb.edu.cn](mailto:wushunchuan@ustb.edu.cn) (S. Wu).

tension, and the critical extension strain criterion only considers the extension crack. The realistic insights of failure processes were mainly deduced from available experimental observations.

In order to retrieve additional information detailing the modes and evolution of damage, the acoustic emission (AE) monitoring techniques have been applied to study the failure processes [13–21]. Acoustic emission (AE) is a high-frequency stress wave generated by the rupture of fractures [18]. AE monitoring has been applied to the monitoring and analysis of the Brazilian tests, and typical cases are summarised as follows. Falls et al. [15] used the two-dimensional AE analysis and ultrasonic velocity imaging to examine stress changes and microfracture activities during the Brazilian test of Lac du Bonnet granite. Labuz et al. [22] conducted diametral compression tests of high strength concrete samples with three-dimensional AE locations. Van De Steen et al. [10] recorded AE locations over time to evaluate the fracture growing in the special configuration (with a hole in the disk). Ohtsu and his co-workers developed the SiGMA (Simplified Green's functions for Moment Tensor Analysis) analysis [23] and applied it to the study of fracture mechanisms in split tensile test of concrete (mortar, normal concrete) [24,25], and then they further applied this to the kinematics of the steel fiber-reinforced concrete and poly-cinyl-alcohol fiber reinforced concrete [26,27]. Rodríguez et al. [28] used three-dimensional localization of AE and AE energy density to characterize the cracking process in marble and monzogranite specimens under diametral compression tests. Liu et al. [29] applied the moment tensor analysis of AE to the Brazilian test of granite and sandstone specimens to study the fracture mechanisms and damage evolution. Zhang et al. [30] studied the three-dimensional evolution of damage in sandstone Brazilian discs by active and passive ultrasonic techniques.

To characterize fracture patterns and identify fracture mechanisms in the Brazilian test, several approaches associated with AE monitoring have been adopted. Falls et al. [15] distinguished different event mechanisms by the amplitude and polarity of the first longitudinal wave motion in different directions with four sensors. This method resembles the moment tensor in two dimensions. Rodríguez et al. [28] combined petrographic with the analysis of AE parameters to improve the characterization of micro cracking of rocks. Ohtsu [19] clarified crack types by SiGMA analysis based on the simplified moment tensor analysis, in addition, this procedure was also used by Liu et al. [29]. Zhang et al. [30] considered the AE events to be associated with the crack initiation mainly consist of tensile and shear microcracks based on the decomposed moment tensors.

It can be seen that the damage evolution process (AE location) and fracture mechanism can be simultaneously obtained from AE records, as long as there are enough sensors (more than 6 sensors in theory, usually 8 sensors in practice). However, there are mainly two difficulties in practical applications of the Brazilian test. First, to obtain the moment tensor, at least 6 sensors have to be used. A moment tensor has nine components, and six of them are independent due to the symmetry of moment tensor. Therefore, at least six sensors are needed to calculate a moment tensor. But six sensors are not sufficient in practice, because an AE event may not trigger all the sensors due to interferences from preexisting cracks, noises, and the coupling effects between the sensors and the specimen. Thus, the best way to improve this is by increasing the number of sensors and optimizing the sensors' spatial configuration. Second, the Brazilian disks are relatively small in size compared to the existing AE sensors. ISRM recommends that the diameter of the Brazilian disk be 50 mm. The Nano-30 sensor used by Liu et al. [29] is 8 mm in diameter, which is relatively small compared to other sensors. However, it is still difficult to place more than 8 such sensors on a disk with a diameter of 50 mm. Therefore, the disks used in the existing studies were quite large, e.g. specimens are of 100 mm diameter and 50 mm thickness by Rodríguez et al. [28], 196 mm diameter and 50 mm thickness by Falls et al. [15], 100 mm diameter and 70 mm thickness by Liu et al. [29] and 150 mm diameter and 100 mm thickness by Mondering and Ohtsu [26]. Moreover, in [29], the mean location error of

AE events was within  $\pm 5$  mm based on the pencil-lead break tests, and in [26], the location errors were within 1.6 mm based on a simulation analysis. Note that the former is related to the availability of moment tensor data, while the latter is about relative error of the results.

As a result, in [26], although more than 1500 hits were detected, only 164 AE events were analyzed. In [21], 1072 AE events triggered a minimum of six sensors, but only 162 events were of sufficiently high quality for moment tensor analysis. Furthermore, Liu et al. [29] and Zhang et al. [30] pointed out that AE signals were missing near the peak load because tens of thousands of waveforms were received in such a short time period, the superposition of numerous AE signals might have diminished the number of located AE events.

In addition, the compression test containing a single flaw is also a typical experiment to study the fracture evaluation. Wong and Xiong examined specimens containing a flaw at different inclination angles [31]. The original size of each specimen is 152 mm  $\times$  78 mm  $\times$  32 mm and 16 Nano-30 sensors are used to monitor the AE from the specimen. Although larger specimen dimension and more sensors are used, the source locations after the peak load deviate greatly from the fracture paths. It indicates that the formation of fractures can affect the propagation of AE signals, which may result in an AE event not being detected by enough sensors. In conclusions, to get precise moment tensor recordings in laboratory -scale rock mechanical tests is still challenging.

However, a numerical approach by which moment tensors of AE events can be calculated was developed [32] and has been successfully applied to simulations of laboratory studies [33,34] and field experiments [32,34]. Therefore, this approach was adopted here for the sake of better understanding of the fracture mechanisms and damage evolution in the Brazilian tests and the compression test with a single flaw.

In this paper, we first introduce numerical modeling approaches, including the contact model and AE simulation in Section 2. In Section 3, AE evolution of the simulated Brazilian test is described, fracture types of AE sources are presented and discussed based on moment tensor inversion, and then AE distribution is compared with stress distribution to explore the underlying fracture mechanism of the Brazilian test. In addition, the AE algorithm is extended to simulate the uniaxial compression test with a single flaw. Finally, failure types of seismic source are discussed in Section 4 and some conclusions are drawn in Section 5.

## 2. Modeling methodology

The algorithm for AE simulation is implemented in the bonded-particle model (BPM) in PFC (Particle Flow Code), which is a branch of explicit discrete element method (DEM) developed by Itasca. Here, particles are assumed to be rigid (non-deformable) and are bonded by contact models which simulate the interaction behavior between particles. Each bond breakage is assumed to be a microcrack, and each microcrack will contribute to seismicity during tests. By monitoring all bond breakages during tests, AE information can be collected and moment tensor (MT) will be calculated for the analyses of fracture type and failure mechanism.

### 2.1. Bonded-particle model

In DEM, two contact models are widely used for the study of intact rock behavior, which are the parallel-bond model (PBM) and the flat-joint model (FJM). In terms of PBM, there are many versions, of which the most notable one is the model described by Potyondy and Cundall [35] (called the standard BPM). However, some limitations are encountered when using the standard BPM: (1) the unrealistically low ratio of the unconfined compressive strength to tensile strength; (2) the low internal friction angle; and (3) the linear strength envelope [36]. Therefore, two main improvements have been made of the standard BPM: (1) a Mohr-Coulomb contact model is employed [37], (2) moment

contribution to bond stress is reduced by introducing a moment-contribution factor ( $\beta \in [0, 1]$ ) [38]. In order to distinguish the above-mentioned models, the improved model is called the enhanced BPM [39].

The limitation of the standard BPM can also be overcome by applying the FJM proposed by Potyondy [40]. There are two main differences between the FJM and PBM: (1) the particles in FJM are polygonal to provide inter-granular interlock; (2) the interface of the FJM is discretized into elements, each element is either bonded or unbonded. The FJM is considered to better characterize the behavior of brittle rock [39] and to supersede the PBM [40]. However, because of the interface discretization in FJM, more than one microcrack may occur at one point. In this AE algorithm, the event centroid (focus) is calculated as the geometrical center of the event, and sensitivity analyses have indicated that the geometric centroid produces satisfactory results [32]. But whether the algorithm is suitable for the FJM remains to be verified. Therefore, the PBM (enhanced BPM) is selected in this research.

## 2.2. AE simulation and moment tensor decomposition

As described in [32], when a bond breaks, the source particles will move and the adjacent contacts will have some deformation. There will therefore be a force change at the surrounding contacts due to the formation of the crack. Components of the moment tensor can be calculated by summing the force change at the contact times the distance of the contact from the crack location. It is worth noting that an AE event can be composed of more than one microcracks. Microcracks occurring close together in space and time are considered as one AE event, and the event centroid is assumed to be the geometrical centre of the event (Fig. 1(a)). The moment tensor can be calculated by integrating around the source boundary, for the discrete element method, the integral is replaced by a sum which is calculated by the following equation:

$$M_{ij} = \sum \Delta F_i R_j \quad (1)$$

where  $\Delta F_i$  is the  $i$ th component of the contact force change and  $R_j$  is the distance between the contact point and event centroid. Since the moment tensor is supposed to be symmetrical, the off-diagonal components of the moment tensor will be assumed to be equal and will be calculated by averaging the two values calculated from the Eq. (1) [32,41]. Besides, the moment tensor is calculated at each timestep during the duration of the AE event, and the single moment tensor stored for each AE event is the result calculated at the timestep of maximum scalar moment [32,42].

A moment tensor can be thought of as the body force equivalent for the source, and the moment tensor representation depicts the principal

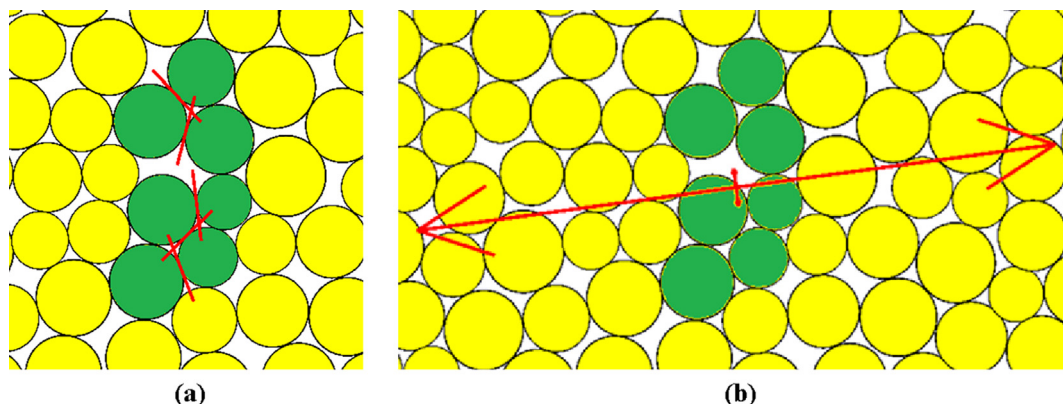


**Fig. 1.** An example AE event composed of 5 single tensile crack. (a) The red segments represent micro cracks and green circles represent source particles. (b) The calculated moment tensor. (For interpretation of the references to color in this figure legend, the reader is referred to the web version of this article.)

values of the moment tensor matrices as two sets of vectors whose direction and length indicate the orientation and magnitude, respectively (Fig. 1(b)).

To identify the fracture mechanism, several ways are proposed for the decomposition of the moment tensor. Two different methods of interpreting moment tensor are usually used in analyses of rocks and rock-like materials. The first way is to classify into tensile crack, shear crack or mixed-mode crack according to the eigenvalue analysis [19]. The following decomposition is obtained as the relative ratios  $X$ ,  $Y$  and  $Z$ ,

$$1.0 = X + Y + Z,$$

The intermediate eigenvalue/the maximum eigenvalue

$$= 0 - Y/2 + Z,$$

The minimum eigenvalue/the maximum eigenvalue

$$= -X - Y/2 + Z;$$

where  $X$  is the shear component,  $Y$  is the deviatoric tensile component and  $Z$  is the hydrostatic mean of tensile. Then a crack is considered as shear with  $X > 60\%$ , as tensile with  $X < 40\%$  and as a mixed mode crack with  $40\% < X < 60\%$  [23,43].

The other way is to divide the moment tensor into isotropic and deviatoric parts:

$$M = \frac{tr(M)}{3} \begin{bmatrix} 1 & 0 & 0 \\ 0 & 1 & 0 \\ 0 & 0 & 1 \end{bmatrix} + \begin{bmatrix} m_1^* & & \\ & m_2^* & \\ & & m_3^* \end{bmatrix} \quad (2)$$

where  $tr(M)$  is the sum of the eigenvalues,  $m_i^*$  are the deviatoric eigenvalues. Crack-types are considered “tensile”, “implosional” or “shear” based on their isotropic ratio which can be calculated by:

$$R = \frac{tr(M) \times 100}{|tr(M) + \sum m_i^*|} \quad (3)$$

The ratio ranges from  $-100\%$  (pure implosion) to  $100\%$  (pure explosion) and  $R = 0$  represents a pure shear failure mechanism. Please refer to Fig. 2 for the schematic diagram of the body-force equivalent. Therefore, a crack is considered “tensile” if  $R > 30\%$ , “implosional” if  $R < -30\%$  and “shear” if  $-30\% < R < 30\%$  [44].

However, the mixed-mode crack in the former one is referred to as the sum of tensile and shear components, whose mechanism is not explicit enough, the latter one is therefore chosen in the present study.

## 2.3. Model descriptions

A granite block, a typical igneous rock, was targeted for the calibration of DEM simulation in this paper. This granite is composed of quartz, feldspar, biotite and a very small amount of iron oxide. A

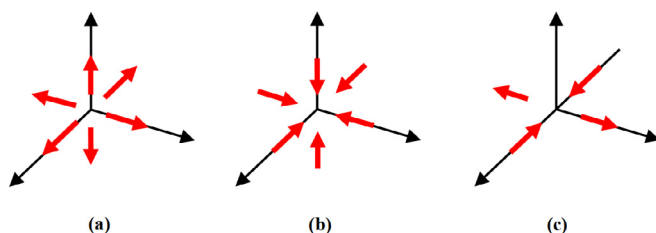


**Fig. 2.** The body-force equivalent for a (a) pure explosive source, (b) pure implosive source and (c) pure shear source. (For interpretation of the references to color in this figure legend, the reader is referred to the web version of this article.)

series of laboratory tests were carried out on this granite, obtaining the density of  $2.8 \text{ g/cm}^3$ , porosity of 0.41% and uniaxial compressive strength of 196 MPa.

A series of Brazilian tests were also conducted, with the sample diameter of 52 mm (D) and thickness of 26 mm (H). Therefore, a disk model of the same geometry was established in PFC and calibrated through trial and error based on the experimental results of granite, shown in Fig. 3. The model parameters used to simulate the granite are listed in Table 1. The installation gap is the ratio of installation gap to minimum particle radius. In terms of the installation gap, contacts can only be generated when the distance between two particles is less than or equal to this value.

Xu et al. [45] stated that the ratio of the Brazilian disk diameter to average grain diameter should be more than 16.7:1 in DEM simulation, while our previous study [46] suggested the ratio should be greater than 20:1 and found that the particle diameter has negligible influence in the simulation of the flattened Brazilian test. Therefore, a relatively small particle diameter was selected. The ratio of the disk diameter to average grain diameter here is about 39:1 and the synthetic Brazilian disk contains 29,191 particles and 134,418 contacts, with an average coordination number of 4.6, ensuring that the AE simulation has enough AE events for the subsequent statistical analysis. The circumference surface was smooth enough, by assigning a small value to the resolution of the cylinder (0.08 in this paper, resolution =  $2\pi/(\text{number of sides of cylinder})$ ), to make sure the disk has a linear contact with the loading walls.

### 3. Results and Interpretation

In both experiments and simulations, the specimen was loaded at a speed of 0.0075 m/s to maintain a quasi-static equilibrium, AE monitoring was active when microcracks occurred. The force-displacement curves from simulation and experiments are shown in Fig. 1(a). The resultant failure patterns in experiments and numerical simulations are

**Table 1**  
Model parameters in the simulation of the granite specimen.

Property	Value
Minimum particle diameter, $d_{\min}$ (mm)	1.0
Ratio of maximum to minimum particle diameter, $d_{\max}/d_{\min}$	1.66
Installation gap ratio, $g_{\text{ratio}}$	0.4
Particle and bond modulus, $E_c = \bar{E}_c$ (GPa)	7
Ratio of normal to shear stiffness of grain and bond, $k_n/k_s = \bar{k}_n/\bar{k}_s$	1.5
Average bond tensile strength with standard deviation, $\sigma_b$ (MPa)	(11, 0)
Average bond cohesion with standard deviation, $c_b$ (MPa)	(110, 0)
Local friction angle, $\phi_b$ (°)	10
Friction coefficient between particles	0.4

compared in Fig. 1(b) and (c).

#### 3.1. Evolution of AE

Loading stopped when the load dropped to 80% of the peak load. Fig. 4(a) shows the force-displacement curve along with the crack number, and Fig. 4(b) shows the force-timestep curve along with AE hits. Along the force-displacement curve, six points labeled A-F were marked, and the load at each point are 20%, 40%, 60%, 80%, 100% and 80% (post-peak) of the peak load respectively. The corresponding points were also marked in Fig. 4(b). It can be seen that before point C there was basically no AE hits before point C in the simulation. It's worth noting that the number of AE events will increase with increasing sample resolution (ratio of particle size to sample size). During stage C-D, the deformation of the disk showed linear elastic behavior and the number of AE hits increased gradually. Afterward, the curve became non-linear, the increment of AE hits accelerated, then the applied force reached to its peak and cracks coalesced. Note there was a little fluctuation before the peak load, subsequently was a trough in the number of AE hits (Fig. 4(b)), which corresponded to the slowly growing of the crack number before the peak load in Fig. 4(a). King et al. [17] indicated that a sudden stress drop occurs when the specimen can no longer sustain the applied load. The large stress drop after the peak load (point E) is the result of the macro-failure throughout the disk, indeed the small stress drop is also accompanied by a large amount of AE hits. Therefore a hypothetical conclusion is drawn that each stress drop during steady loading will lead to the emergence of large amount of AE hits.

The location of AE events are drawn by stages to demonstrate the evolution process of AE sources (Fig. 5). The diameter of the circles are proportional to the magnitude of AE events and the color of the circles reflects the crack type of AE events. The red circles represent implosive sources, the green circles represent shear sources, and the blue circles

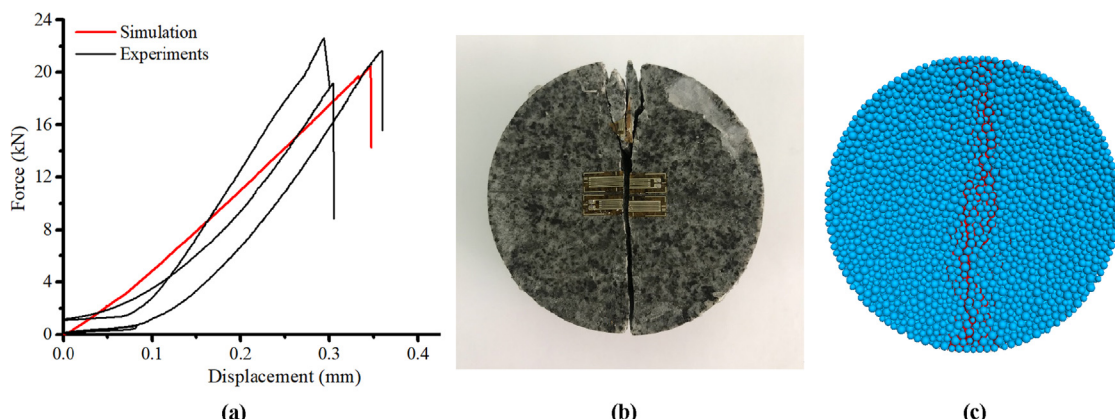


**Fig. 3.** Results of the Brazilian tests, (a) force-displacement curves from experiments (black lines) and simulation (red line), and a typical failure specimen from (b) experiments and (c) simulations. (For interpretation of the references to color in this figure legend, the reader is referred to the web version of this article.)

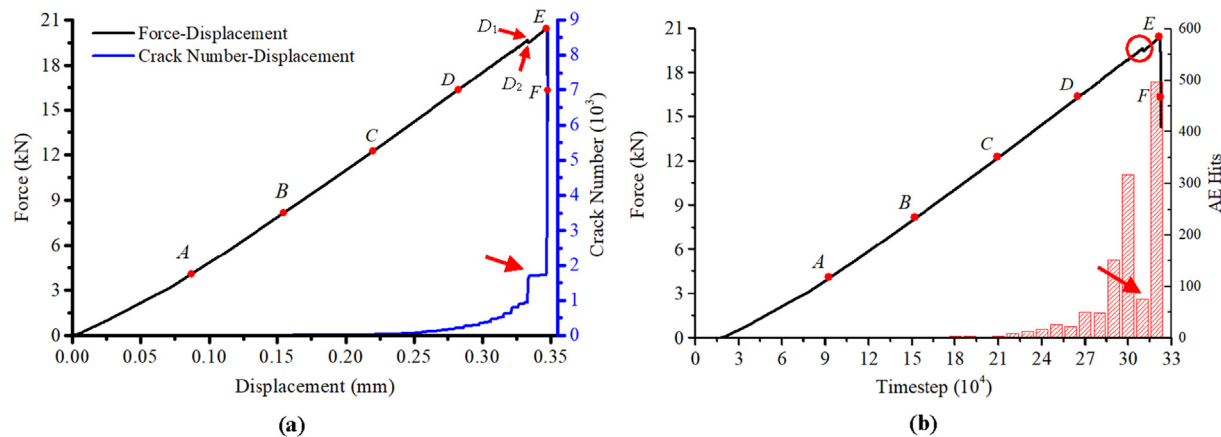


**Fig. 4.** Force and AE behavior in the Brazilian test simulation, (a) force-displacement curve and cumulative crack number, (b) the number of AE hits along the force-timestep curve.

represent explosive sources (tensile cracks). During stage A-B, only three tensile AE events with small radius occurred near the lower loading plane. Then in stage B-C, AE events also appeared near the upper loading plane, and shear sources began to appear. The asymmetry of AE type is caused by the heterogeneity of the specimen. Later, crack initiation was observed at about 80% of the peak load, represented by a few AE events concentrated in the vicinity of the loading points. Besides, cracks tended to spread to the center of the disk. After that, during the stage D-E, AE responses became active, and AE hits increased stably and spread across the compression diameter, with the arrival of the peak load. Finally, the disk split along the loading axis, accompanied by more AE events with large magnitude.

A large number of AE events occurred in stage D-E so that the detailed extension process of AE cannot be clearly observed. The

fluctuation before the peak leads to the appearance of a local peak and a local nadir. Thus, the local peak and local nadir are marked as  $D_1$  and  $D_2$  (see Fig. 2), respectively. As shown in Fig. 6, AE events mainly concentrated between loading ends and the center of the disk before point  $D_1$ . Then, the force-displacement curve reached its local peak point (point  $D_1$ ), and subsequently an accelerated phase of AE events started. Intuitively, substantial AE events appeared within only 1000 timesteps (compared to the entire process of more than  $3 \times 10^5$  timesteps, 1000 timesteps is significantly short) accompanied with a small stress drop. After that, the force risesd stably again, however, only a few AE events occurred near the central part of the disk before the peak load (point E).

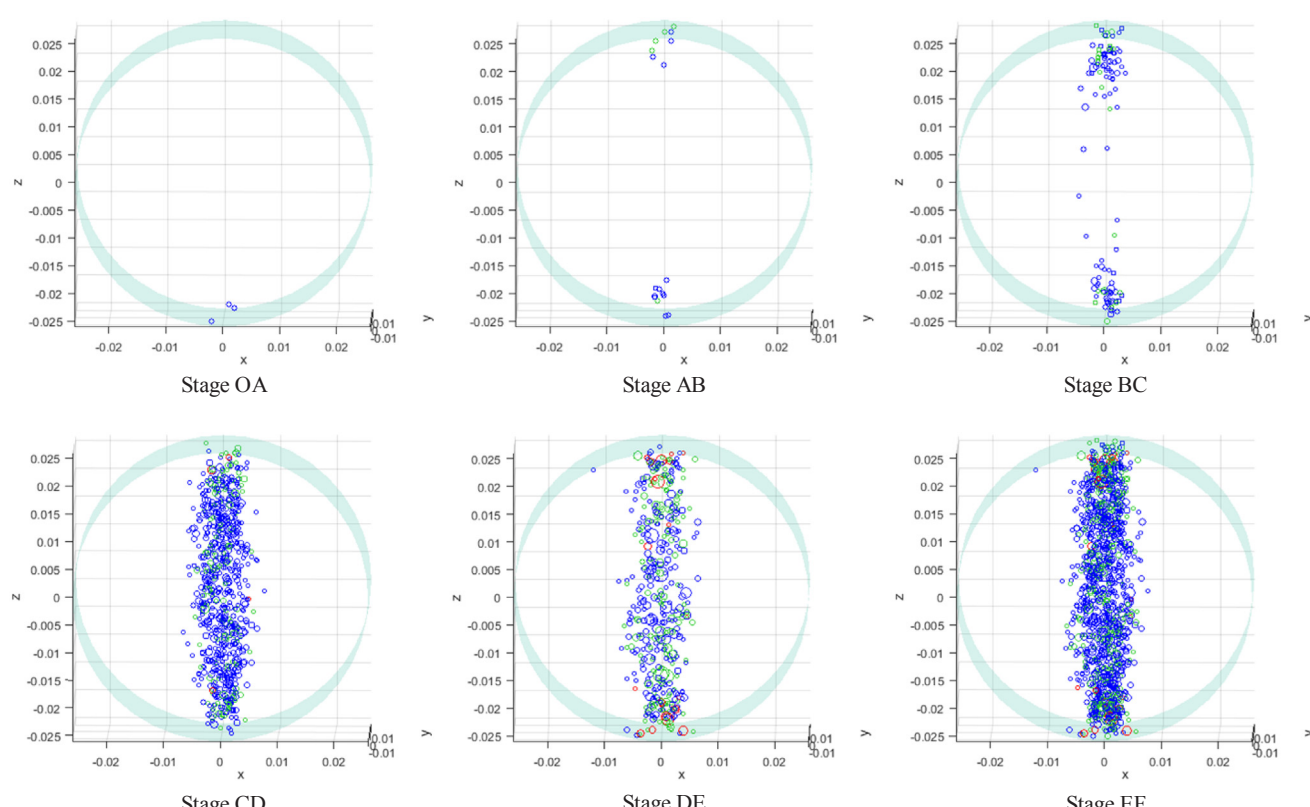


**Fig. 5.** Distribution of AE event during each stage, red circles represent implosive sources, green circles represent shear sources, and the blue circles represent explosive sources. (For interpretation of the references to color in this figure legend, the reader is referred to the web version of this article.)

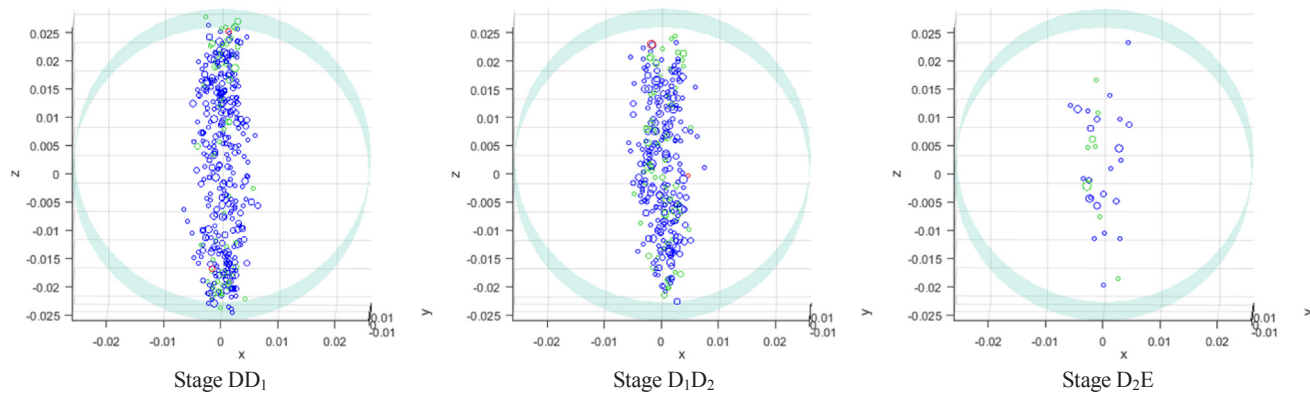


**Fig. 6.** Detailed AE evolution processes during stage D-E.

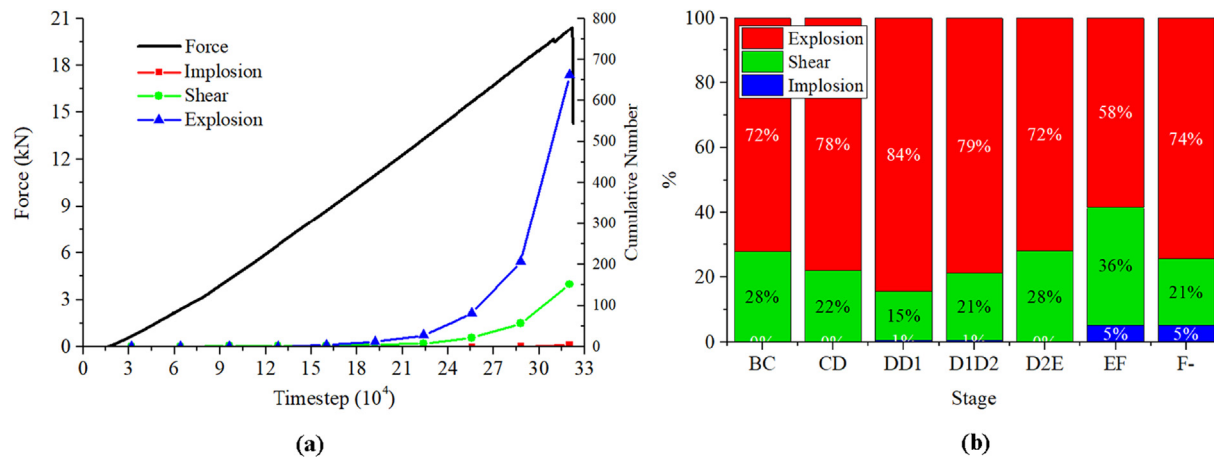


**Fig. 7.** Source types based on the decomposition of moment tensors, (a) cumulative number of each type along the force-timestep curve, (b) percentages of each type during different stages.

### 3.2. Fracture types of AE sources

To investigate the fracture type of AE sources during rock failure, the number of each type and their ratio are counted. Fig. 7 shows the cumulative number changing of three AE source types with the force-timestep curve. It is shown that slopes of the cumulative curves slope of shear and explosion increase over time, which means the frequencies of these two source types increase over time (i.e., increase with the increasing applied load). But the AE number of implosion is too small to conclude. There are only 27 implosion AE events and most of them (23 implosion events) occurred after the peak load. During the whole loading process, explosive sources, namely the tensile meso-cracks, occupied the dominant position, and the ultimate explosion percentage reached about 81% in number. However, the ratio of explosive source reached its minimum value in stage E-F (only 58% at the post-peak phase), while shear source reached the maximum (36%). In terms of the shear source (Fig. 7(b)), the ratio of number appeared to decrease first and then increase. At the initial stage, the relatively high ratio of shear sources was the result of stress distribution inside the Brazilian disk. It has been found that an early shear failure crack occasionally occurred due to the stress concentration under the loading ends [1,47]. In addition, Van De Steen et al. [10] proposed that fracturing in the Brazilian test is initiated in shear in the vicinity of one of the platens and subsequently grows in tension by conducting the diametrical loading test with a hole. This phenomenon obtained from the moment tensor analysis is consistent with the conclusion drawn from analytical and experimental analyses that the number ratio of shear sources will decline at first. As for the post-peak phase, the maximum shear proportion may result from the unstable crack growth and the coalescence between

micro tensile cracks. Besides, the disk has split into two halves, the abrasions induced by the relative slide between fragments on the macro-crack also contributed to observed shear sources. That is the reason why the largest share of the shear sources appeared at the post-peak phase during the Brazilian test.

In terms of the implosive source, only 27 implosive events (2.1% of the total) occurred during the whole test, and most of them (23 events) occurred at the post-peak phase (5% at stage E-F). In PFC, the particles are assumed to be rigid, but still some approaches have been proposed to simulate intragranular damage [48,49], for example, modeling the rock as an assemblage of “clusters” made up of bonded particles, or allowing the particles to split within the grain. Such intergranular damage and pore collapse are the main mechanism of the origin of the implosive source in practice. However, this mechanism usually occurs under high confining pressure or with high porosity. Therefore, in the simulation of Brazilian test (no confining pressure), there is no need to adopt such complex approaches mentioned above. Hazzard and Young [32,34] have stated the formation of the implosive event in PFC that although the implosive event is mainly composed of micro tensile cracks, the surrounding particles will move in to fill the space vacated by the tensile cracking. That also explains why most implosive events occurred at the post-peak phase because the formed macro tensile crack led to the surrounding particles being pushed inwards to compensate for the volume change. If the intergranular damage is considered, the implosion ratio may account for more.

The locations of three types of events are shown respectively in Fig. 8 with the radius proportional to the magnitude. Circles are colored according to the origin time in timestep since the start of the simulation, the lighter the color, the later it appears. Circles are plotted with

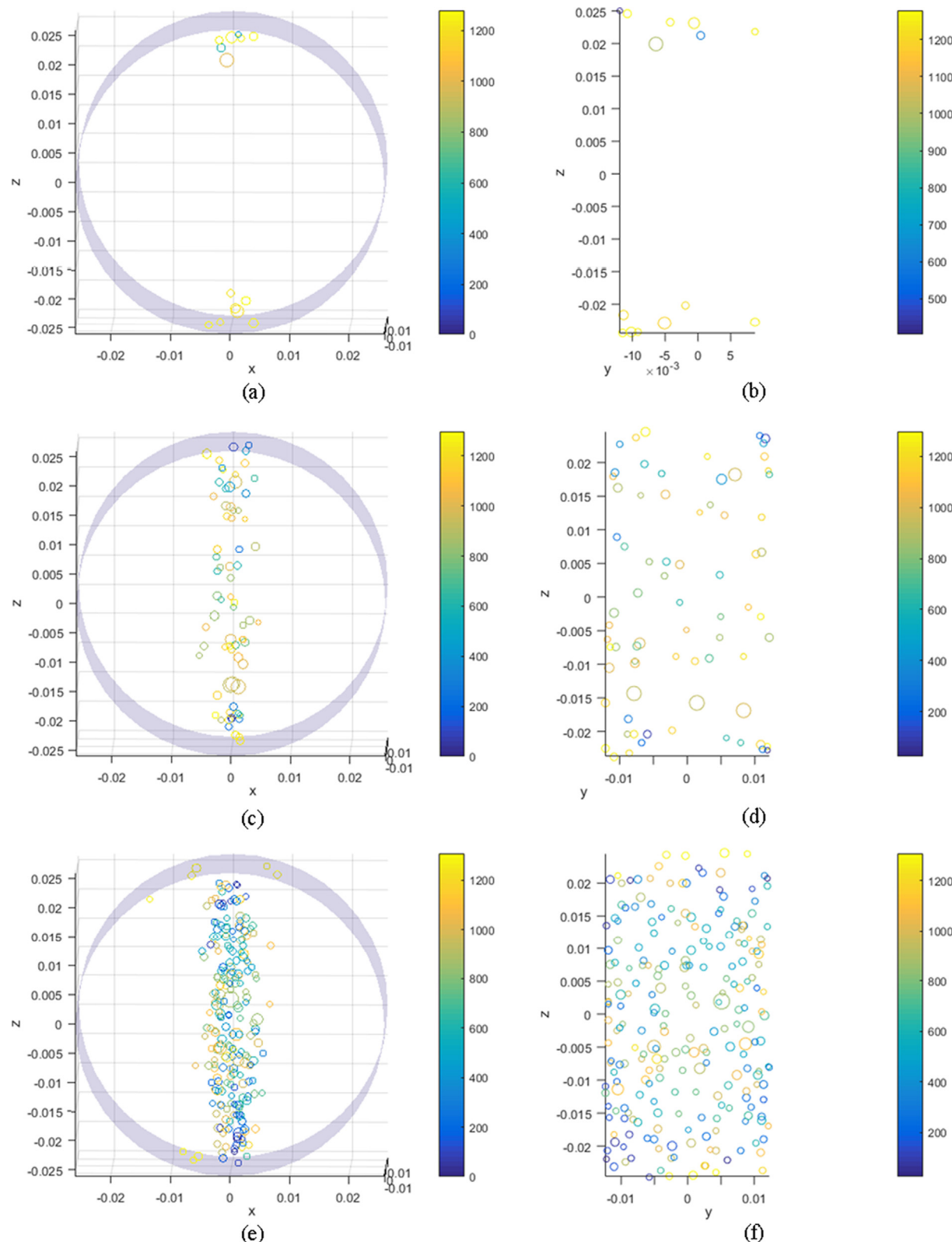


**Fig. 8.** AE evolution processes of different source types: (a) front view of implosive events, (b) side view of implosive events, (c) front view of shear events, (d) side view of shear events, (e) front view of explosive events, (f) side view of explosive events. Radii of circles are proportional to the magnitude, and colors of circles reflect the origin timestep of AE events, the lighter the color, the later it appears.

large overlaps because basically all the events are localized along the loading diameter, so that events cannot be clearly identified. Thus, events with small magnitude are ignored, namely, only events consisted of more than 2 microcracks are plotted. It can be seen that the implosive

events all localized near the loading ends and occurred nearly the end of the test. Shear events distributed along the loading diameter, and events with large magnitude mainly happened about 10 mm away from the lower loading plate. Explosive events also mainly distributed over

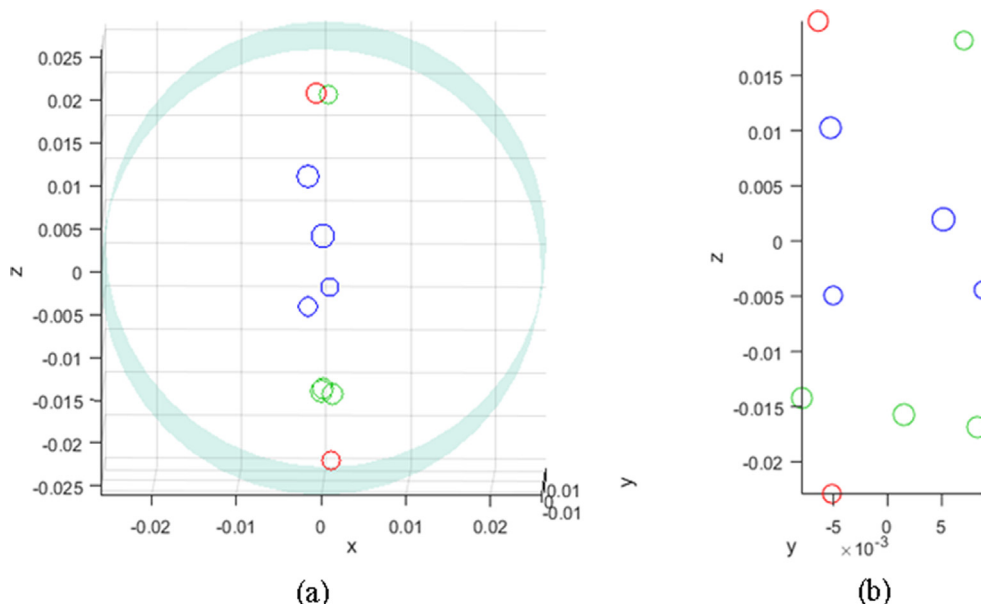


**Fig. 9.** Localization of ten largest AE events, two implosive sources (red), four shear sources (green) and four explosive sources (blue) (a) front view and (b) side view. (For interpretation of the references to color in this figure legend, the reader is referred to the web version of this article.)

the loading diameter, with some appeared at the circumferential surface near two loading ends. Although the number of explosion is the largest, most of them are of small magnitude. In practice, the precision of specimen processing and the error of loading instruments may have an effect on the experimental results. In experiments, it is found that AE hits mainly localized near one end surface in a granite Brazilian disk [29]. However, in simulation, all kinds of events were evenly distributed along the axis direction of the disk, because processing error and loading error can be well controlled. The results of AE simulation are relatively accurate, and therefore it can be used as a supplement approach to experiments contributing to the qualitative interpretation of AE monitoring.

### 3.3. Fracture mechanism based on moment tensor inversion

In order to study the distribution of three types of AE sources, the ten largest events of magnitude were screened out, including four explosive events, four shear events and two implosive events. Each of these ten events contains more than 100 microcracks, of which the largest one is an explosive event consisting of 1069 microcracks. It can be seen from Fig. 9 that the distribution of the three types of events has certain regularity. Explosions were mainly in the vicinity of the center of the disk, on the contrary implosions occurred near the loading ends, and shear events localized between the two. The asymmetry of AE events between the upper and lower parts of the disk might be ascribed to the heterogeneity of the specimen, however, the regularity of three types of sources is definitely controlled by stress distribution in the disk.

To investigate the correlation between AE distribution and stress distribution, a series of measurement regions were arranged along the loading diameter. The horizontal stress in each measurement region was recorded and connected with a smooth curve. For comparison, the stress distribution was also calculated using FEM (ANSYS) (Fig. 10). It is found that the maximum tensile stress value occurs on the specimen surface [12], therefore, only the stresses on the surface plane along the loading diameter were demonstrated. The results from DEM and FEM are illustrated in Fig. 11. Although the curve obtained from DEM contains certain fluctuations, the whole trend is resembled to that of the FEM. It can be seen that the horizontal tensile stresses are basically uniformly distributed in the vicinity of the center of the disk ( $-18 \text{ mm}$  to  $18 \text{ mm}$  in vertical direction), in addition, the compressive stresses are

extremely large near two loading ends ( $23\text{--}25 \text{ mm}$  and  $-23 \text{ to } -25 \text{ mm}$  in vertical direction). Therefore, it is easy to explain why explosions mainly occurred in the vicinity of the center of the disk and implosions occurred near the loading plates. Apart from this, although the stress distribution is the fundamental cause of AE distribution, conventional stress analysis can only analyze the initiation of cracks, while AE monitoring can analyze the entire process of fracture.

There is no doubt that the crack initiation point is located near the loading point in the Brazilian test for rocks. Initially, it was assumed that the crack should initiate from the center of the Brazilian disk based on the Griffith criterion. The crack initiation point was found to occur away from the center of the disk [1,45,47,50]. The crack initiation point of the Brazilian test has been intensively investigated, however, the mechanism of crack initiation has not yet been unified because different strength criteria have different emphases. In terms of the moment tensor inversion results, events with large magnitude (high energy release) were basically shear sources at crack initiation points, although the explosive events were dominant in quantity at the crack initiation points. The fracture mechanism inverted from moment tensor is consistent well with the results of [10].

However, the classification of AE sources as an explosive source, a shear source or an implosive source suggests not a pure tensile crack, a pure shear crack or a pure crushing crack, respectively. The largest ten events are represented in the Hudson  $T$ - $k$  plot [51], which provides a graphical plot of source mechanism types (Fig. 12). Explosive and implosive sources have certain shear components, while shear sources also have certain implosive components.

### 3.4. Comparison with experimental results

For comparison with experimental results, AE behavior of granite disc [29] is targeted in the present study. The model is  $100 \text{ mm}$  in diameter and  $70 \text{ mm}$  in height, the micro parameters are calibrated based on the numerical results. Liu et al. [29] classified AE events into tensile cracks, shear cracks and mixed-mode cracks using Ohtsu's method [23], while AE events were divided into tensile cracks, shear cracks and implosion cracks based on Feignier and Young's classification [44]. Although classifications are different, they are both based on the same moment tensor decomposition theory, and both tensile cracks and shear cracks are contained. Thus, the number and energy release of

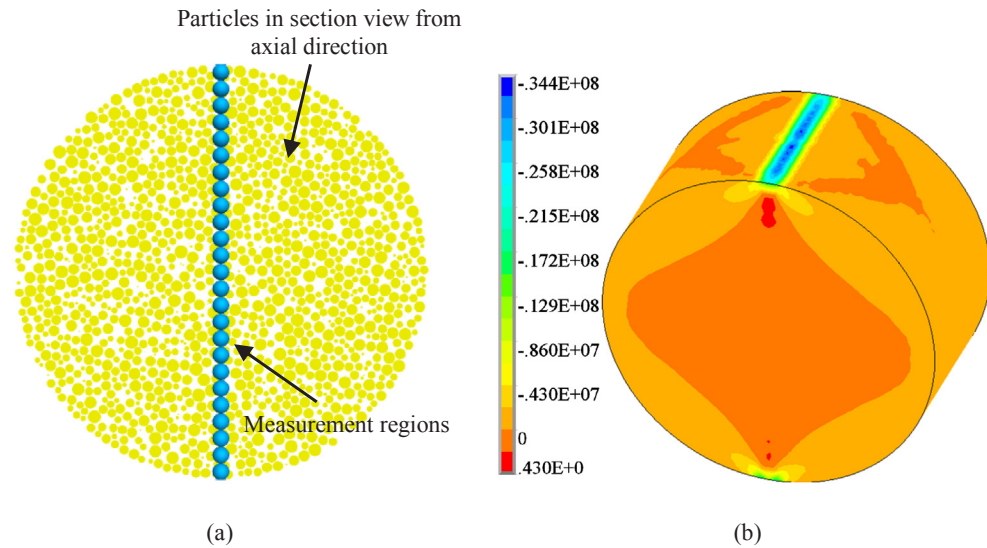


**Fig. 10.** (a) Measurement regions in the sectional view in PFC, (b) horizontal stress nephogram in ANSYS.

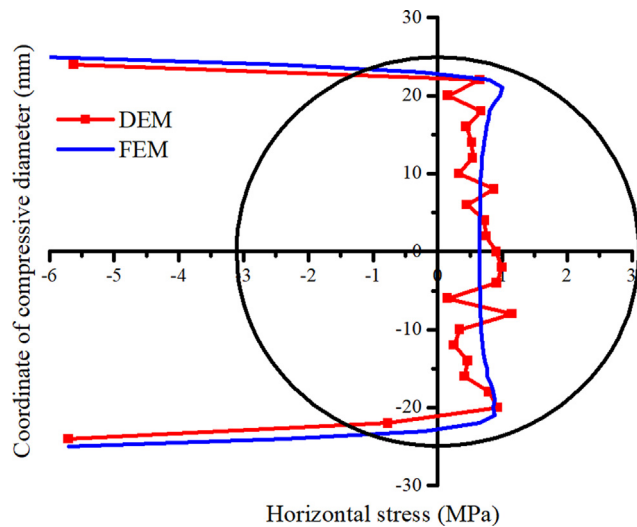


**Fig. 11.** Horizontal stress distributions along the loading diameter in the Brazilian disk obtained from DEM (red line) and FEM (blue line). (For interpretation of the references to color in this figure legend, the reader is referred to the web version of this article.)

tensile cracks and shear cracks are compared in this section.

The relations between loads and AE hits are illustrated in Fig. 13. Though the stress-strain curves from the experiment and simulation are a little different, the evolution processes of AE responses are similar. In the initial stage, only a few AE events were detected and increased gradually. Then AE hits rapidly grow subsequently the applied force reached its peak. Finally, AE hits increased dramatically which led to the macro failure of the disc.

The evolution of crack number and energy release for different kinds of cracks are illustrated in Fig. 14. It's worth noting that Fig. 14(a) depicts only the data before peak load, while Fig. 14(b) contains a set of post-peak data. Both the number and energy release of different kinds of crack increased with increasing applied force before peak load. The tensile cracks played a dominant role in both cracks number and energy emission during the whole loading processes, then shear cracks and followed by implosions.

By contrast, the force-displacement curve from the simulation appears linear. This may be due to the lack of primary voids and some inherent defects in DEM. In experiments, when the Brazilian disk was

loaded, the original openings tended to close which resulted in the non-linear stress-strain behavior. Regardless of this, the failure process and AE behavior coincided reasonably well with experiments.

### 3.5. Applications to other sample geometry

Fracture processes and crack patterns in pre-cracked samples have been widely studied on different materials. In this section, the uniaxial compression test with a single flaw is simulated with the MT algorithm. Fracture processes and crack patterns in pre-cracked samples have been widely studied on different materials. The specimen was generating according to [31] which is 152 mm × 78 mm, the flaw is designed to be 13 mm in length, 1.6 mm in aperture and 30° from horizontal. The specimen contains 51,913 particles with radii ranging from 0.4 mm to 0.6 mm. The flaw is created by imported geometry in the model center to ensure the smoothness of the flaw surface. The specimen is loaded by a constant strain rate of 0.01 s<sup>-1</sup>, and MT information is recorded during the whole loading process. A total of about 3700 AE events were detected. The AE hits densities are first plotted into histograms against timesteps (Fig. 15), then the whole test is separated into different stages based AE hits density buildups and drops. AE locations and types of different stages are presented separately in Fig. 16(a-f), and the corresponding microcrack distributions are shown in Fig. 17 (top).

As shown in Fig. 16(a), except for a few small AE events randomly distribute over the specimen which may be caused by the pre-existing defects, tensile AE events concentrate near the flaw tips, which are called tensile wing cracks [52] or primary cracks [53,54]. Then, wing cracks extend slightly while anti-wing cracks (the term secondary crack is used in [53,54] to describe this kind of crack) begin to appear in Fig. 16(b). From Fig. 16(c)-(f), both wing cracks and anti-wing cracks remarkably widen and extend to upper and lower specimen boundaries as loading continues, which lead to macro failure of the specimen.

For comparison, experimental AE results and corresponding screenshots from [31] are shown in Fig. 16(g) and Fig. 17 (bottom), respectively. In experiment, the AE clusters and white paths match closely before the white patches reach the specimen boundaries and become open (the white patch is the trace before crack opening, please refer to Ref. [31] and Fig. 17 (bottom)). However afterward, AE source location becomes scattered and large errors occurred. It is because wave propagation and the coupling between sensors and the specimen are affected by cracks. It is expectable that the accuracy of AE location decreases with the increasing number of microcracks. This speculation is coincident with the experimental phenomenon. As shown in

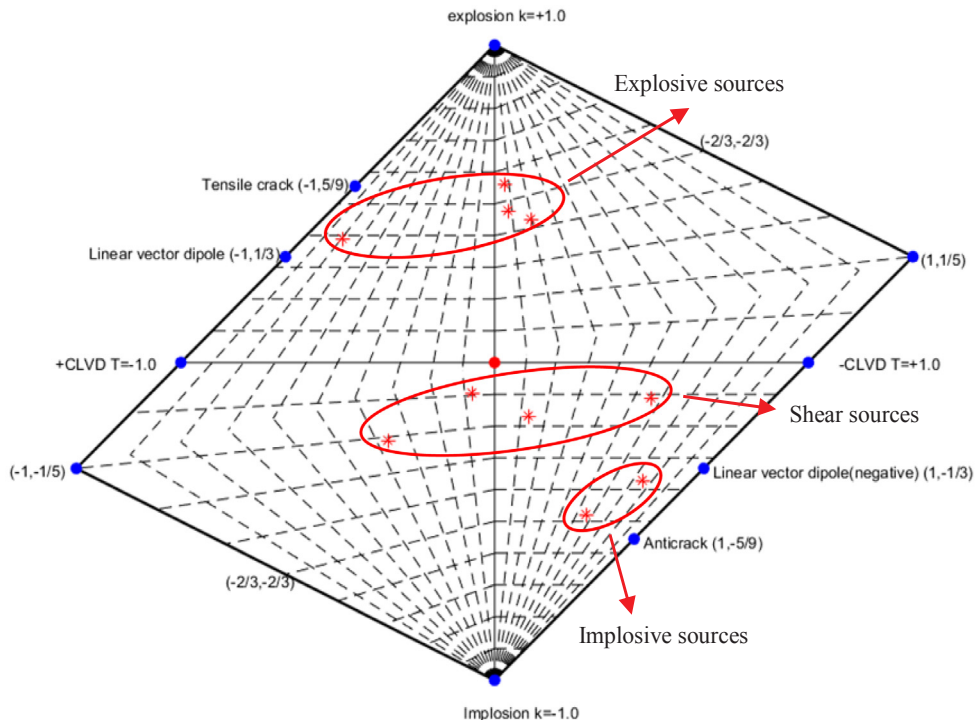


**Fig. 12.** Hudson  $T$ - $K$  plot of the ten largest AE events.

**Fig. 16(g)**, AE clusters concentrated at flaw tips when wing cracks initiated, while they had a certain distance from the crack tips when anti-wing cracks occurred. This is inconsistent with the screenshot by camera (**Fig. 17** (bottom)).

In terms of moment tensor inversion, the simulated AE results are different from those in experiments. It can be seen from **Fig. 16(g)** that shear cracks play the dominant role during the whole test. However, in the present study, wing cracks initiate in tensile while anti-wing cracks initiate and propagate into both shear and tensile failures. Results in the present study are more comparable with previous studies on crack propagation [52–54]. Moment tensor inversion results are affected by the accuracy of AE locations. Some errors in the laboratory scale test are inevitable but really matter to results. Therefore, AE simulation is a good assistant approach in crack initiation and propagation study.

#### 4. Discussion

To identify the failure type of seismic source, the moment tensors are usually decomposed into the isotropic (ISO), double-couple (DC) and compensated linear vector dipole (CLVD) components. Although

the crack classifications by Liu et al. [29] and the present study are different, both are based on the same moment tensor decomposition method. The difference, however, is that the present study considered the percentage of ISO component while Liu et al. [29] considered the percentage of DC component. In the study of rock mechanics, only tensile cracks and shear cracks are generally considered. Nonetheless, implosion failures have been observed in tunnel excavation [55] and mining situations [56]. The implosive events in geotechnical engineering are considered to be induced by closure of cracks and collapse of excavation holes. In the simulation of intact rock, there are no pre-cracks and void defects considered. In addition, the particles in the present model are assumed to be rigid which are not allowed to deform and further fracture in the present model. Therefore, to investigate the mechanism of implosion in this simulation, the evolution through time of a single implosive event is presented in the  $T$ - $k$  plot, in **Fig. 15**.

This implosive event lasted for about 45  $\mu$ s and consisted of more than 300 micro-cracks. Three time steps are selected during this event, i.e., at 6.1  $\mu$ s, 19.1  $\mu$ s and the end of this implosive event (**Fig. 18**). At 6.1  $\mu$ s, this event is composed of 11 micro-cracks which has large positive isotropic component. As time progresses, the moment tensor

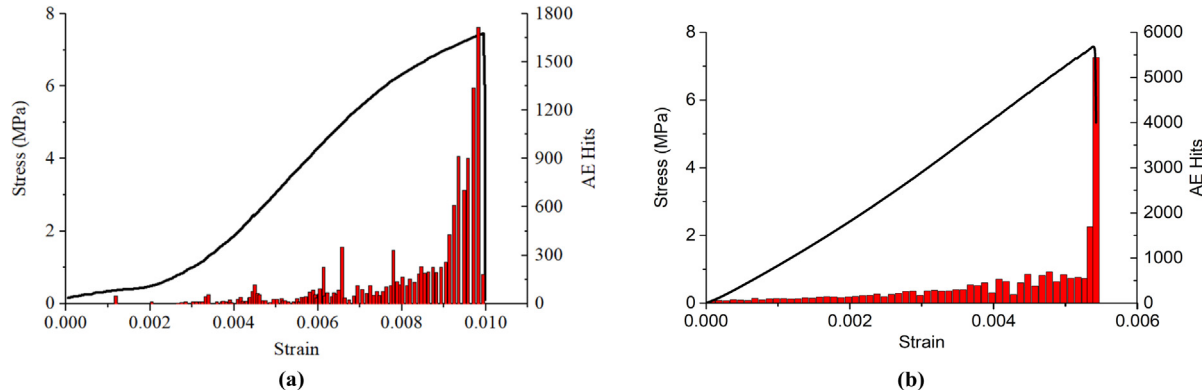


**Fig. 13.** AE hits along stress-strain curves of (a) experiment [29]; (b) present simulation.

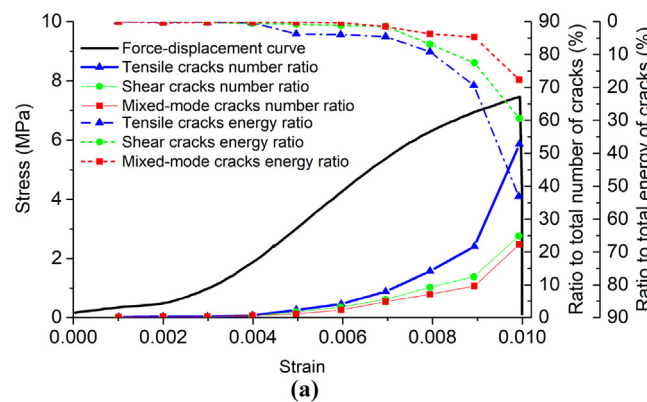


Fig. 14. Ratios of crack number and energy release for different kinds of cracks along the stress-strain curves, (a) experiment [29], (b) simulation.

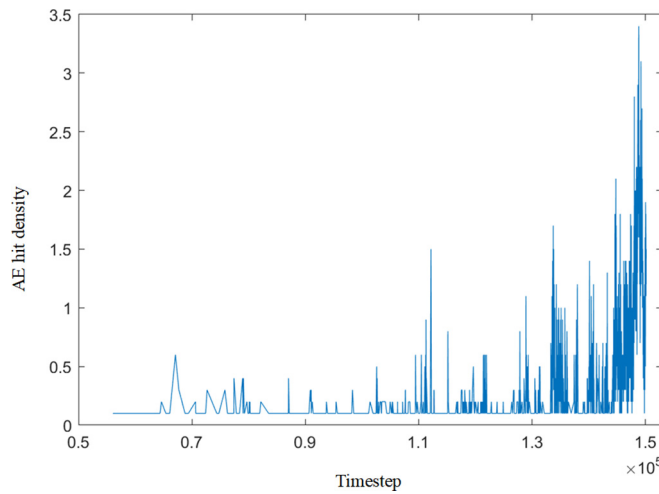
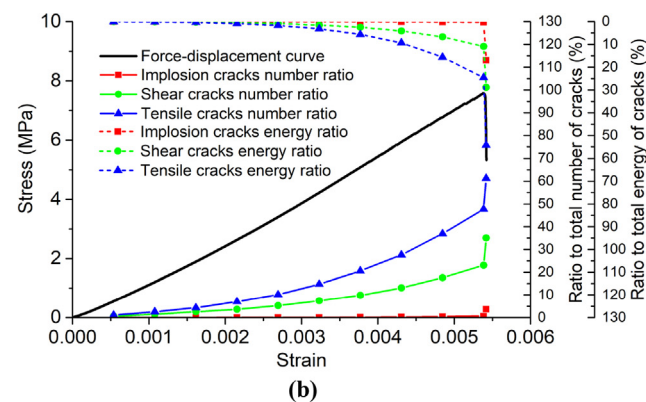


Fig. 15. Histogram plot of AE hits density.

becomes a double couple source and finally displays a predominantly implosive mode. It is worth noting that the moment tensor describes the equivalent body force, but the same equivalent force does not necessarily indicate the same failure mode. A double couple can represent a shear failure, but it may also be a tensile crack caused by compression perpendicular to it. Therefore, it can be inferred that particles injecting into tensile cracks finally leads to the negative isotropic component.

Compared to experiments, MT simulation can record data from the post-peak part and also compensate for limited accuracy in experiments, especially for samples with small dimensions. In the present simulation, the ten largest AE events all occurred at the post-peak part which eventually led to the macro crack. The errors of AE location and moment tensors in experiments are inevitable, and these errors are usually caused by noise, the determination of P-wave arrival time and approximation for Green's functions [21,29]. Sometimes, the located AE events even occurred outside the specimen, especially for specimen with small dimensions [30]. Many methods have been used to mitigate this problem, such as machine learning of wave discrimination [57]. However, moment tensors in the present simulations were directly calculated by the forces and motions of the particles, so the results can be used as the labelled training dataset, excluding the imperfection of the measured data.

Moreover, after the current study focusing on validating the modeling, further large-scale AE simulations can provide substantial data for machine learning (the rules induction algorithm) to predict microseismic hazard, which can lead to better hazard identification and thus contributing to better prevention and mitigation of hazards [58]. In conclusion, the implementation of AE simulation can supplement the understand of micromechanics of rock failure and provide training data



to meta-learning for accurate predictions of microseismic hazards.

## 5. Conclusions

AE monitoring simulation was employed in the enhanced BPM to investigate the damage evolution process during the Brazilian test and the compression test with a single flaw. The moment tensors of AE events were directly calculated by the forces and motions of the particles at the sources for the cognition of fracture mechanism during simulations.

It can be seen from the failure process during the Brazilian test that cracks initiated about 5 mm away from the loading ends then propagated to the center of the disk. There were only a few AE hits in the initial stage, then AE hits rapidly grow before the applied force reached its peak. AE events first concentrated in the vicinity of the loading ends, and subsequently propagated towards the central part of the disk. In addition, every stress drop was accompanied by a large number of AE hits.

Explosive sources (tensile cracks) were dominant both in number and energy release during the whole simulation of the Brazilian test, followed by shear sources and finally implosive sources. At crack initiation point, though tensile cracks were dominant in number, events with large magnitude were basically shear sources. Therefore, it can be concluded that in the Brazilian test cracks are initiated in shear near loading ends, then propagate towards the disk center which finally leads to a macro-tensile crack at the central part of the disk accompanied by crushing at loading points (implosive sources).

AE distribution and MT inversion can reflect the stress distribution inside the specimen. The stress distribution is the inducement of crack initiation and propagation, and is also the inducement of AE inversion. Both stress distribution in DEM and FEM were presented in this paper and compared with AE distribution and MT inversion. The positions of AE events are where the stresses exceed the bond strength, namely the stress concentration points, the magnitude of AE event represents the intensity of stress concentration, and the fracture type of AE event reflects the type of stress in a certain region.

AE simulation was also applied into uniaxial compression test with a single flaw. The simulated AE results coincide well with the failure process in experiments. Both the AE source locations and the MT inversion results are more comparable with experimental phenomenon than laboratory scale AE results. It can be concluded that the AE simulation algorithm can make up for the insufficient source location accuracy and the MT inversion is an effective and accurate way to study the fracture mechanism of rock failure.

## CRediT authorship contribution statement

**Jun Ma:** Conceptualization, Software, Formal analysis, Data curation, Investigation, Writing - original draft. **Shunchuan Wu:**

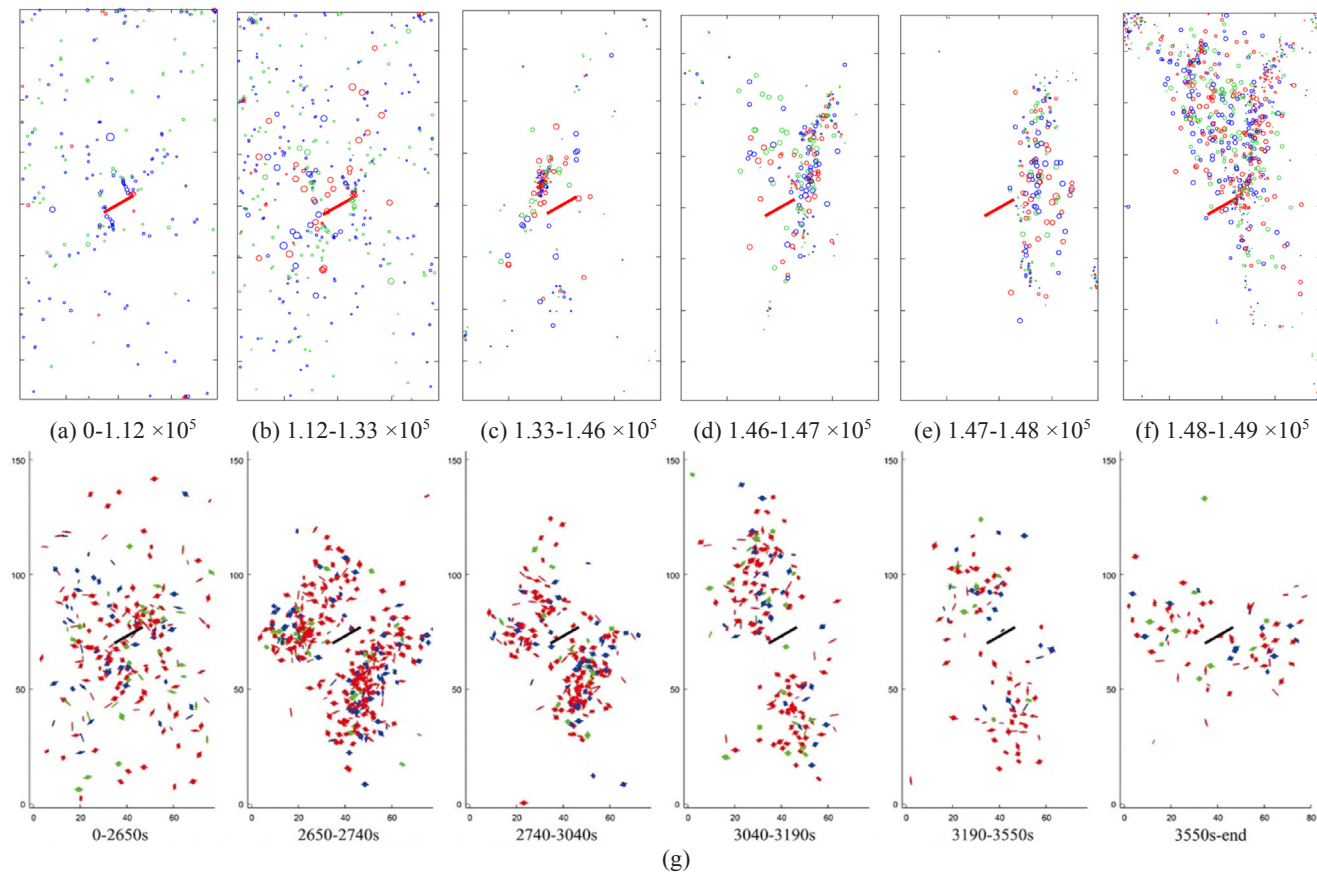


**Fig. 16.** (a–f) Numerical AE source location and MT inversion results of each stage, red, green and blue circles represent implosive sources, shear sources and explosive sources, respectively; (g) experimental AE source locations and moment tensor inversion results [31].

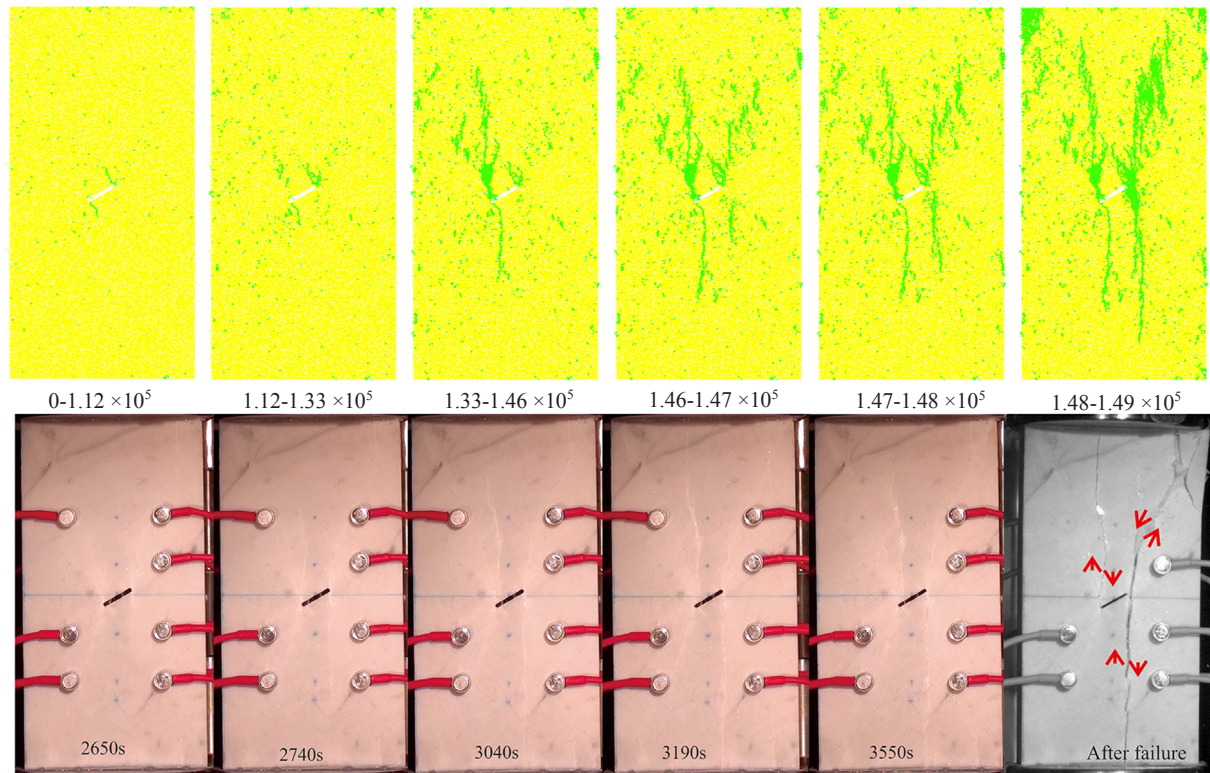


**Fig. 17.** (top) Microcrack distributions at the end of each stage, (bottom) screenshots by high-speed camera from experiments [31].

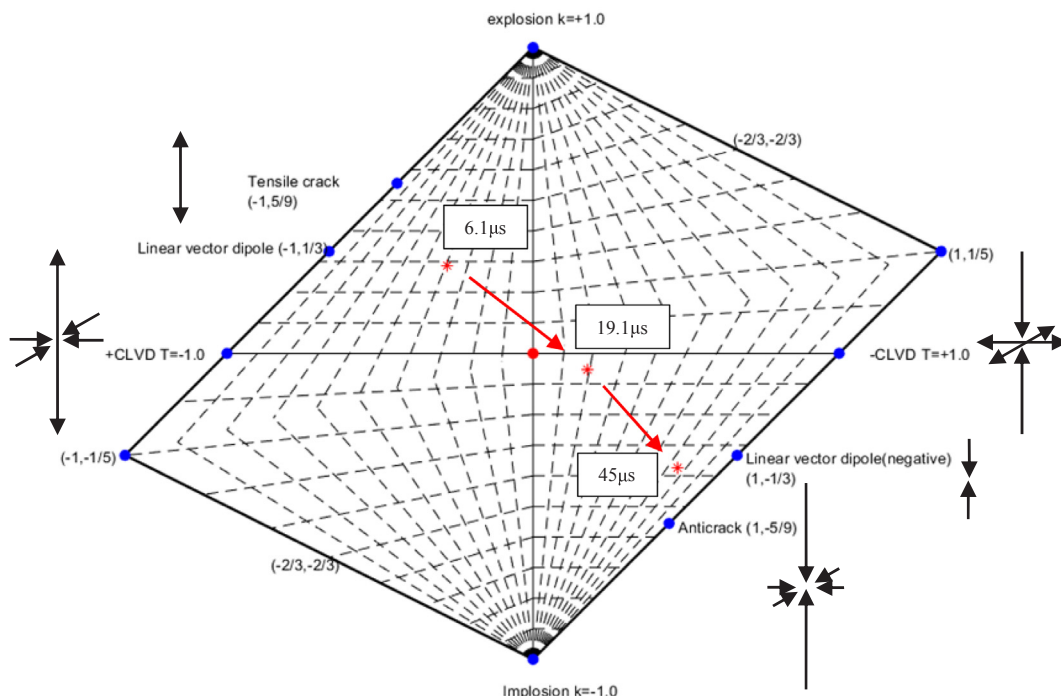


**Fig. 18.** The T-k value of an implosive event at different time, this event first shows positive isotropic component, then becomes a double couple source and finally displays aimplosive mode.

Supervision, Methodology, Software, Resources, Funding acquisition. **Xiao-Ping Zhang:** Methodology, Writing - review & editing. **Yixiang Gan:** Investigation, Visualization, Validation, Writing - review & editing.

#### Declaration of Competing Interest

The authors declare that they have no known competing financial interests or personal relationships that could have appeared to influence the work reported in this paper.

#### Acknowledgments

The supports received from the National Natural Science Foundation of China (51934003, 51774020) and Program for High-level Introduced Talent Innovation Team of Yunnan Province are gratefully acknowledged. The first author gratefully acknowledges financial support from China Scholarship Council.

#### References

- [1] Fairhurst C. On the validity of the 'Brazilian' test for brittle materials. *Int J Rock Mech Min Sci Geomech Abstr* 1964;1:535–46.
- [2] Coville A, Lagioia R, Nova R. On the measurement of the tensile strength of soft rocks. *Rock Mech Rock Eng* 2005;38:251–73. <https://doi.org/10.1007/s00603-005-0054-7>.
- [3] Yu Y, Zhang J, Zhang J. A modified Brazilian disk tension test. *Int J Rock Mech Min Sci* 2009;46:421–5. <https://doi.org/10.1016/j.ijrmms.2008.04.008>.
- [4] Fuenkajorn K, Klanphumeesri S. Laboratory determination of direct tensile strength and deformability of intact rocks. *Geotech Test* 2011;34:97–102. <https://doi.org/10.1520/GTJ103134>.
- [5] Andreew GE. A review of the Brazilian test for rock tensile strength determination. Part I: calculation formula. *Min Sci Technol* 1991;13:445–56. [https://doi.org/10.1016/0167-9031\(91\)91006-4](https://doi.org/10.1016/0167-9031(91)91006-4).
- [6] Mellor M, Hawkes I. Measurement of tensile strength by diametral compression of discs and annuli. *Eng Geol* 1971;5:173–225. [https://doi.org/10.1016/0013-7952\(71\)90001-9](https://doi.org/10.1016/0013-7952(71)90001-9).
- [7] Pandey P, Singh DP. Deformation of a rock in different tensile tests. *Eng Geol* 1986;22:281–92. [https://doi.org/10.1016/0013-7952\(86\)90029-3](https://doi.org/10.1016/0013-7952(86)90029-3).
- [8] Efimov VP. The rock strength in different tension conditions. *J Min Sci* 2009;45:569–75. <https://doi.org/10.1007/s10913-009-0071-0>.
- [9] Diederichs MS. A review of the tensile strength of rock: concepts and testing. *Geotech Geol Eng* 2014;32:525–46. <https://doi.org/10.1007/s10706-014-9732-0>.
- [10] Van De Steen B, Vervoort A, Napier JAL. Observed and simulated fracture pattern in diametrically loaded discs of rock material. *Int J Fract* 2005;131:35–52. <https://doi.org/10.1007/s10704-004-3177-z>.
- [11] Lanaro F, Sato T, Stephansson O. Microcrack modelling of Brazilian tensile tests with the boundary element method. *Int J Rock Mech Min Sci* 2009;46:450–61. <https://doi.org/10.1016/j.ijrmms.2008.11.007>.
- [12] Li DY, Wong LNY. The Brazilian disc test for rock mechanics applications: review and new insights. *Rock Mech Rock Eng* 2013;46:269–87. <https://doi.org/10.1007/s00603-012-0257-7>.
- [13] Lockner D, Byerlee J, Kuksenko V, Ponomarev A, Sidorin A. Quasi-static fault growth and shear fracture energy in granite. *Nature* 1991;350:39–42.
- [14] Vajdova V, Wong TF. Incremental propagation of discrete compaction bands: acoustic emission and microstructural observations on circumferentially notched samples of Bentheim. *Geophys Res Lett* 2003;30. <https://doi.org/10.1029/2003GL017750>.
- [15] Falls SD, Young RP, Hutchins DA. Acoustic emission analysis and ultrasonic velocity imaging in the study of rock failure. *J Acoust Emiss* 1989;8:166–9. <https://doi.org/10.1520/STP19108S>. ASTM International.
- [16] Townend E, Thompson BD, Benson PM, Meredith PG, Baud P, Young RP. Imaging compaction band propagation in Diemelstadt sandstone using acoustic emission locations. *Geophys Res Lett* 2008;35. <https://doi.org/10.1029/2008GL034723>.
- [17] King MS, Pettitt WS, Haycox JR, Young RP. Acoustic emissions associated with the formation of fracture sets in sandstone under polaxial stress conditions. *Geophys Prospect* 2012;60:93–102. <https://doi.org/10.1111/j.1365-2478.2011.00959.x>.
- [18] Goodfellow SD, Young RP. A laboratory acoustic emission experiment under in situ conditions. *Geophys Res Lett* 2014;41:3422–30. <https://doi.org/10.1002/2014GL059965>.
- [19] Ohtsu M. Simplified moment tensor analysis and unified decomposition of acoustic-emission source - application to in situ hydrofracturing test. *J Geophys Res Earth Planets* 1991;96:6211–21. <https://doi.org/10.1029/90jb02689>.
- [20] Ohtsu M, Ohtsuka M. Damage evolution by acoustic emission in the fracture process zone of concrete. *Doboku Gakkai Ronbunshu* 1998;1998:177–84.
- [21] Aker E, Kühn D, Vavryčuk V, Soldal M, Oye V. Experimental investigation of acoustic emissions and their moment tensors in rock during failure. *Int J Rock Mech Min Sci* 2014;70:286–95. <https://doi.org/10.1016/j.ijrmms.2014.05.003>.
- [22] Labuz JF, Cattaneo S, Chen LH. Acoustic emission at failure in quasi-brittle materials. *Constr Build Mater* 2001;15:225–33. [https://doi.org/10.1016/S0950-0618\(00\)00072-6](https://doi.org/10.1016/S0950-0618(00)00072-6).
- [23] Ohtsu M. Acoustic emission theory for moment tensor analysis. *Res Nondestr Eval* 1995;6:169–84. <https://doi.org/10.1007/BF01606380>.
- [24] Ohtsu M, Kawasaki Y. AE-SiGMA analysis in Brazilian test and accelerated corrosion test of concrete. *J Acoust Emiss* 2010;28:204–14.
- [25] Mondoringin M, Nozaki S, Ohtsu M. AE-SiGMA analysis in Brazilian test of concrete. *Concr Res Lett* 2012;2:2009–12.
- [26] Mondoringin MRIAJ, Ohtsu M. Kinematics on split-tensile test of fiber-reinforced concrete by AE. *J Adv Concr Technol* 2013;11:196–205. <https://doi.org/10.3151/2013.11.196-205>.

- jact.11.196.
- [27] Mondorinig MR, Ohtsu M. Ae-sigma analysis in split-tensile test of fiber-reinforced concrete (Frc) at meso-scale. *J Ilm Media Eng* 2015;5.
- [28] Rodríguez P, Arab PB, Celestino TB. Characterization of rock cracking patterns in diametral compression tests by acoustic emission and petrographic analysis. *Int J Rock Mech Min Sci* 2016;83:73–85. <https://doi.org/10.1016/j.ijrmms.2015.12.017>.
- [29] Liu Q, Liu Q, Pan Y, Liu X, Kong X, Deng P. Microcracking mechanism analysis of rock failure in diametral compression tests. *J Mater Civ Eng* 2018;30:4018082. [https://doi.org/10.1061/\(ASCE\)MT.1943-5533.0002251](https://doi.org/10.1061/(ASCE)MT.1943-5533.0002251).
- [30] Zhang S, Wu S, Zhang G, Guo P, Chu C. Three-dimensional evolution of damage in sandstone Brazilian discs by the concurrent use of active and passive ultrasonic techniques. *Acta Geotech* 2018;1–16.
- [31] Wong LNY, Xiong Q. A method for multiscale interpretation of fracture processes in Carrara marble specimen containing a single flaw under uniaxial compression. *J Geophys Res Solid Earth* 2018;123:6459–90.
- [32] Hazzard JF, Young RP. Moment tensors and micromechanical models. *Tectonophysics* 2002;356:181–97. [https://doi.org/10.1016/S0040-1951\(02\)00384-0](https://doi.org/10.1016/S0040-1951(02)00384-0).
- [33] Al-Busaidi A, Hazzard JF, Young RP. Distinct element modeling of hydraulically fractured Lac du Bonnet granite. *J Geophys Res Solid Earth* 2005;110:1–14. <https://doi.org/10.1029/2004JB003297>.
- [34] Hazzard JF, Young RP. Dynamic modelling of induced seismicity. *Int J Rock Mech Min Sci* 2004;41:1365–76. <https://doi.org/10.1016/j.ijrmms.2004.09.005>.
- [35] Potyondy DO, Cundall PA. A bonded-particle model for rock. *Int J Rock Mech Min Sci* 2004;41:1329–64.
- [36] Wu S, Xu X. A study of three intrinsic problems of the classic discrete element method using flat-joint model. *Rock Mech Rock Eng* 2016;49:1813–30. <https://doi.org/10.1007/s00603-015-0890-z>.
- [37] Wang Y, Tonon F. Modeling Lac du Bonnet granite using a discrete element model. *Int J Rock Mech Min Sci* 2009;46:1124–35. <https://doi.org/10.1016/j.ijrmms.2009.05.008>.
- [38] Potyondy DO. Parallel-bond refinements to match macroproperties of hard rock. In: 2nd FLAC/DEM Symp., 2011, p. 14–6.
- [39] Vallejos JA, Salinas JM, Delonca A, Mas Ivars D. Calibration and verification of two bonded-particle models for simulation of intact rock behavior. *Int J Geomech* 2016;17:06016030. [https://doi.org/10.1061/\(ASCE\)GM.1943-5622.0000773](https://doi.org/10.1061/(ASCE)GM.1943-5622.0000773).
- [40] Potyondy DO. A flat-jointed bonded-particle material for hard rock. In: 46th US Rock Mech. Symp., 2012, p. 10.
- [41] Zhang X-P, Zhang Q. Distinction of crack nature in brittle rock-like materials: a numerical study based on moment tensors. *Rock Mech Rock Eng* 2017;50:2837–45.
- [42] Zhao XP, Young RP. Numerical modeling of seismicity induced by fluid injection in naturally fractured reservoirs. *Geophysics* 2011;76:Wc167–80. <https://doi.org/10.1190/Geo2011-0025.1>.
- [43] Ohno K, Ohtsu M. Crack classification in concrete based on acoustic emission. *Constr Build Mater* 2010;24:2339–46.
- [44] Feignier B, Young RP. Moment tensor inversion of induced microseismic events: evidence of non-shear failure in the -4 < M < -2 moment magnitude range. *Geophys Res Lett* 1992;19:1503–6.
- [45] Xu X, Wu S, Gao Y, Xu M. Effects of micro-structure and micro-parameters on Brazilian tensile strength using flat-joint model. *Rock Mech Rock Eng* 2016;49:3575–95. <https://doi.org/10.1007/s00603-016-1021-1>.
- [46] Wu S, Ma J, Cheng Y, Xu M, Huang X. Numerical analysis of the flattened Brazilian test: failure process, recommended geometric parameters and loading conditions. *Eng Fract Mech* 2018;204:288–305.
- [47] Hudson JA, Brown ET, Rummel F. The controlled failure of rock discs and rings loaded in diametral compression. *Int J Rock Mech Min Sci* 1972;9:241–4. [https://doi.org/10.1016/0148-9062\(72\)90025-3](https://doi.org/10.1016/0148-9062(72)90025-3).
- [48] Wang B, Chen Y, Wong TF. A discrete element model for the development of compaction localization in granular rock. *J Geophys Res Solid Earth* 2008;113. <https://doi.org/10.1029/2006JB004501>.
- [49] Li L, Holt RM. Particle scale reservoir mechanics.pdf. *Oil Gas Sci Technol* 2002;57:525–38.
- [50] Swab JJ, Jian Y, Gamble R, Kilczewski S. Analysis of the diametral compression method for determining the tensile strength of transparent magnesium aluminate spinel. *Int J Fract* 2011;172:182–92.
- [51] Hudson J, Pearce RRR. Source type plot for inversion of the moment tensor. *J Geophys Res* 1989;94:765–74.
- [52] Wong LNY, Einstein HH. Systematic evaluation of cracking behavior in specimens containing single flaws under uniaxial compression. *Int J Rock Mech Min Sci* 2009;46:239–49.
- [53] Ingraffea AR, Heuze FE. Finite element models for rock fracture mechanics. *Int J Numer Anal Methods Geomech* 1980;4:25–43.
- [54] Chen G, Kemeny JM, Harpalani S. Fracture propagation and coalescence in marble plates with pre-cut notches under compression. *Fract Jointed Rock Masses* 1995;435–9.
- [55] Baker C, Young RP. Evidence for extensile crack initiation in point source time-dependent moment tensor solutions. *Bull Seismol Soc Am* 1997;87:1442–53.
- [56] McGarr A. An impulsive component in the seismic moment tensor of a mining-induced tremor. *Geophys Res Lett* 1992;19:1579–82. <https://doi.org/10.1029/92GL01581>.
- [57] Li Z, Meier MA, Hauksson E, Zhan Z, Andrews J. Machine learning seismic wave discrimination: application to earthquake early warning. *Geophys Res Lett* 2018;45:4773–9. <https://doi.org/10.1029/2018GL077870>.
- [58] Sikora M. Induction and pruning of classification rules for prediction of micro-seismic hazards in coal mines. *Expert Syst Appl* 2011;38:6748–58. <https://doi.org/10.1016/j.eswa.2010.11.059>.